Final Draft
of the original manuscript:

Experimental and numerical lifetime assessment of Al 2024 sheet

S. Khan, O. Kintzel, J. Mosler*

Helmholtz-Zentrum Geesthacht, Institute of Materials Research, Materials Mechanics, Max-Planck-Str. 1, 21502 Geesthacht, Germany

Abstract

In the present paper, a thorough analysis of the low-cycle fatigue behavior of flat sheets of aluminum Al 2024-T351 is given. For that purpose, material characterization is combined with material modeling. The experimental analyses include monotonic and cyclic loading tests at high stress levels. For the assessment of microstructural characteristics, advanced imaging technology is used to reveal, e.g. crack initiation loci and particle sizing. The numerical simulation is done using a novel ductile-brittle damage model. Thereby, the model parameters are optimized by means of an inverse parameter identification strategy which, overall, leads to a very good agreement between experimentally observed and computationally predicted data. For demonstrating the prediction capability of the novel coupled model also for complex engineering problems, a certain stringer assembly, as used in fuselage parts of airplanes, is analyzed.

Keywords: Low cycle fatigue, continuum damage mechanics (CDM), aluminum alloys, ductile damage

1. Introduction

High-performance metallic sheets show a broad range of industrial applications. For example, (i) stainless steel plates are used in ship manufacturing and (ii) high-strength aluminum alloys are employed in the aviation and automotive industry. More specifically, high-strength aluminum alloys, such as Al 2024-T351, are widely used for lightweight structural applications, especially in transportation vehicles. In the aerospace industry, they are utilized in the form of sheets and plates in the fuselage or the lower wing.

Because of the growing demands on the critical performance of machines and constructions, and due to an emphasis on the economy of production, it is generally accepted that many structures need not to be, or even cannot be, designed for infinite life. The design must, however, ensure that the expected lifetime of the structure is reached and the desired safety is achieved. In any case, knowledge of the prospective lifetime of a component is of enormous practical interest. For the prediction of the lifetime, the consideration of low-cycle fatigue is of special significance, since repeated loading under high stress amplitudes limits the service lifetime of many highly-stressed components like those used in the fuselage or gas turbine engines in aircrafts severely.

At the microstructural level, low-cycle fatigue is caused by accumulation of micro-damage. In ductile metallic materials like steels and aluminum, microvoid nucleation and growth have been recognized as key mechanisms of damage. Analyzing the elongation of spherical or elliptical voids in a porous medium, Mc Clintock [1] and Rice and Tracey [2] initiated the research on void growth laws. Afterwards, many new developments in

this field contributed to a number of ductile damage models or failure criteria. Today, the approaches are numerous and can be sorted broadly into three main classes : (i) abrupt failure criteria, (ii) porous metal plasticity, and (iii) continuum damage mechanics (CDM) approaches. For the first mentioned modeling approach, ductile failure is assumed when a micromechanical variable, for instance the cavity growth, cf. Rice et al. [3], reaches a critical characteristic material value. Regarding the second approach, damage effects are accounted for by a softening of the yield limit in dependence on the amount of porosity, cf. [4, 5, 6].

Finally, in the CDM approach, originated in the early works of Kachanov [7], softening effects associated with material damage are considered by means of thermodynamic internal state variables. In this framework, in contrast to porous plasticity theory, damage effects are accounted for by a degradation of material moduli like the elastic stiffness. Mathematically speaking, this method is based on a smeared representation of the initiation, growth and coalescence of micro-defects and/or micro-cracks. Integrated within a thermodynamics framework, CDM models use as many internal state variables as there are mechanisms of deformation and material degradation to be accounted for, cf. [8, 9].

Recently, a novel model suitable for the analysis of low cycle fatigue in high-strength aluminum alloys was proposed in [12]. This model is based on careful experiments and material characterization of a thick plate of Al 2024-T351, see [10, 11]. Within the results reported in [10, 11], a broad variety of different damage mechanisms ranging from ductile to quasi-brittle could be observed for loading in S-direction (thickness direction). This complex mechanical response is captured by the model discussed in [12] by combining a ductile damage model originally advocated in [13] with a novel approach for quasi-

brittle material degradation.

Although the material characterization of thick plates in S-direction is indeed important for understanding the complex mechanical response of Al 2024-T351, most practically relevant applications are based on thin sheets. For this reason, such sheets are analyzed in the present paper. More precisely, the present contribution addresses a microstructural analysis of flat specimens of Al 2024-T351 under cyclic loading conditions, the identification of failure and damage mechanisms and their prediction by numerical methods. The corresponding microstructural characterizations are carried out with the aid of quantitative image analysis, yielding the morphology of grains and particles within the material. With fractography, the basic mechanisms of failure are identified. For the accompanying numerical simulations, the model proposed in [12] is adopted. The respective material parameters are optimized by means of an inverse parameter identification strategy. For that purpose, standard flat tensile specimens are considered. Finally, the calibrated material model is used for predicting crack initiation in a complex engineering structure. As a representative example, a stringer-skin connection of a fuselage is chosen.

2. Material characterization and experimental setup

The high-strength aluminum alloy considered in the present study belongs to the Al-Cu alloy family. Such alloys are specifically designed for their superior mechanical properties for use in critical structural parts of aircrafts. They contain copper (Cu) as major alloying element and hardening is achieved by aging. The material used in this work is a hot-rolled sheet of Al 2024, as received in a T351 temper (solution heat treated, air-quenched, stress-relieved by cold stretching). The chemical composition is given in Tab. 1.

Table 1: Composition (wt %) of Al 2024-T351 by chemical analysis

Cu	Mg	Mn	Si	Fe	Cr	Al
4.11	1.12	0.46	0.048	0.05	0.003	Rest

In order to characterize the alloy's mechanical behavior, tests have been done on two different sources, a plate of 100 mm and a sheet of 4 mm thickness. Extensive work has already been done on the plate, see [10, 11, 12], where in particular the short-transversal (thickness) direction was the main focus of interest. While the material response along the plate dimensions of the thick plate is rather uniform and can be characterized as ductile, a quasi-brittle material behavior could be identified in thickness direction, see [12]. In the present paper, the damage mechanisms in flat sheets of Al 2024-T351 are analyzed. For these analyses, specimens were machined from a sheet of 4.0 mm thickness in two directions with respect to the rolling direction, namely

- L: Longitudinal

- T: Transversal, i.e. perpendicular to the rolling direction.

Within the cyclic loading experiments, symmetric strain amplitudes (R=-1) have been used. Consequently, large compressive stresses occur. For avoiding buckling under a negative strain ratio, the shape of the flat specimens has been carefully chosen, cf. [15]. The shape and the dimensions of the specimen are depicted in Fig. 1. After fabrication, the edges of the specimen were reworked by hand using a cylindrical abrasive pencil and polished lengthwise especially around the notches using a rubbing compound to prevent initial edge cracks.
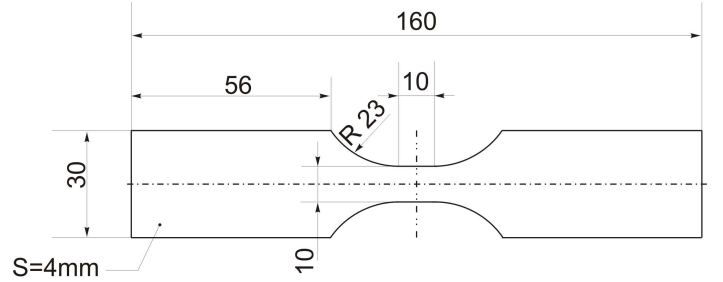

Figure 1: Specimen geometry used in the tests

The monotonic tensile tests were performed under displacement control using a mechanical Zwick Roell 1484 testing machine (maximum force 200 kN) with a constant cross head speed of 0.5 mm/min, while the cyclic tests were done on a Schenck 160 kN servo-hydraulic testing machine. Grips were carefully aligned with the aid of an alignment fixture. An extensometer with gauge length of 8 mm, laterally attached to the specimen, was used to measure length changes, since the measurement of cross-head travel was not appropriate. Another reason for attaching a clip-gauge across the specimen is the possibility of obtaining high resolution displacement data close to the region of interest. It should be mentioned that the damage localization loci were always inside the respective gauge length. Load-displacement responses were recorded using DASYLab^{TM} software. The stress was determined as ratio between the clamp force to the (undeformed) cross-sectional area at the center of the specimen, i.e., engineering stresses were used.

The cyclic tests were conducted at room temperature with triangular loading increments at a standard frequency 0.01 Hz with fully reverse control of the strain amplitude (R=-1). This very low frequency was chosen in order to obtain a better resolution of the load-displacement curve. During the experiments, the instant of mesocrack initiation was assumed at the moment of a sudden drop of the maximum cyclic peak load, cf. [11].

The determination of fatigue properties in thin sheets is extremely problematic due to a high risk of buckling of the sheet during compression, cf. [16, 17]. Although the specimen's geometry has been chosen carefully, an anti-buckling guide was additionally used to prevent buckling, allowing the specimen to "lean" against the guide without buckling. A floating guide technique was used for that purpose, see Fig. 2. A teflon (PTFE) lubrication film of 0.5 mm thickness was inserted between the buckling guides at both sides of the specimen. By these means it could be ensured, that the axial freedom of movement of the
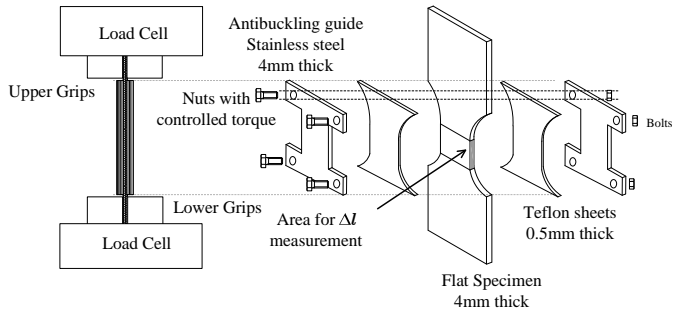
Figure 2: Anti-buckling support for LCF experiments, the extensometer (gauge length 8mm) is attached to the edges of the specimen

specimen was constrained as little as technically possible while at the same time buckling could be prevented. For confirming this hypothesis, an experimental test series was done where only the first half-cycle at the highest amplitude (both in T- and L-direction) was compared to a monotonic tensile test without the anti-buckling guide. As evident from Fig. 3, the macroscopic behavior is indeed not disturbed profoundly by the use of the anti-buckling guide.
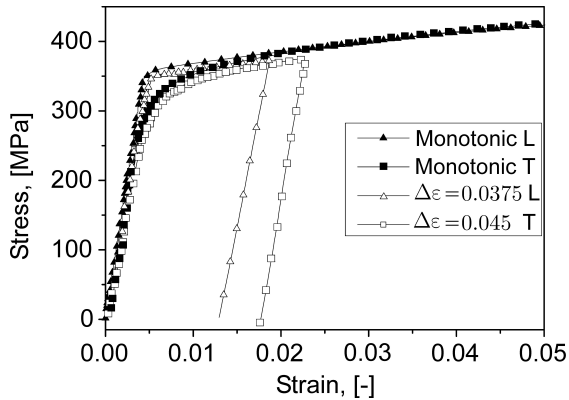

Figure 3: Independence of the experiments of the anti-buckling guide: macroscopic behavior during the first half-cycle of a cyclic test using the anti-buckling guide compared to that of the monotonic tensile test without the anti-buckling guide

2.1. Microstructure

The mechanical anisotropy of metals is strongly related to the spatial distribution of grain orientations, grain shapes and sizes. While orientations of grains can in principle be determined by texture measurements, sizes and shapes of the grains become visible by polishing and etching plane cross-sections of the material. Photographs have been taken of all three different surfaces using polarized light, having its normal vectors in L-, T- and S-direction, respectively. Fig. 4(a) shows the locations and orientations of the test specimens taken and 4(b) displays the grain structure, showing the material anisotropy of the sheet with elongated grains along the L-T-planes. While the average grain sizes in L- and T-directions are 20 μm and 10 μm, respectively, the grain dimensions across the thickness of the sheet are

reduced due to the rolling process and measure on average only 5 μm. Clearly, since the loading is applied across the plane of the sheet, the mechanical properties are primarily influenced by the orientation of the grains along this plane, having roughly an aspect-ratio of 2 with respect to the T- and L- directions.
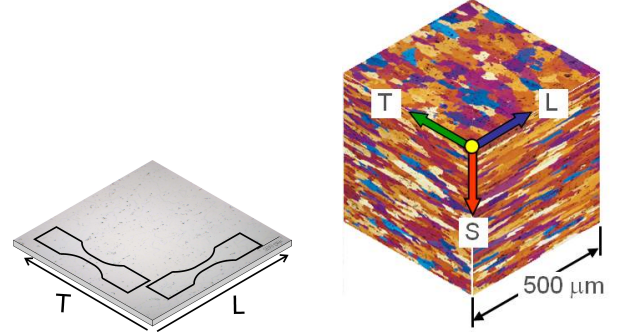

Figure 4: a) Location and orientation of the specimens; b) microstructure of Al 2024 sheet material (magnified)

Typically, the presence of intermetallic particles, which act as void nucleation sites, determines the damage tolerance of a material. Here, these heterogeneous particles are distributed spatially in clusters through the length and thickness of the material. In contrast to thick plates, these particles do not vary much in their dimensions, cf. [10, 11, 12].

2.2. Results – Experiments

Tab. 2 summarizes the characteristic quantities obtained from the uni-axial tensile tests of the material in the following loading directions of the sheet: L (longitudinal), D (45°) and T (transversal). Accordingly, the L-specimens show a higher value of yield stress, ultimate stress and total elongation. In all tests, the ductility is fairly similar. The strain at fracture lies between 0.31 and 0.29, where the highest value has been measured in L-direction. For the related stress quantities, engineering stresses have been calculated, taking the minimum area at the center of the specimen.

Table 2: Mechanical properties of Al 2024 T351 (monotonic loading, 3 samples considered in averaging)

Tensile direction	Yield stress [MPa]	Tensile Strength [MPa]	Fracture strain [-]
L	365	473	0.31
T	321	468	0.30
D	318	468	0.29

Additionally, cyclic deformation experiments at constant strain range $\Delta\epsilon$ were also performed. The complete characterization of the material response requires the continuous monitoring of the stress amplitude. During the initial phase of cyclic deformation, (rapid) cyclic hardening occurs, giving rise to an increase in peak stresses σ_p, followed by an extended regime of
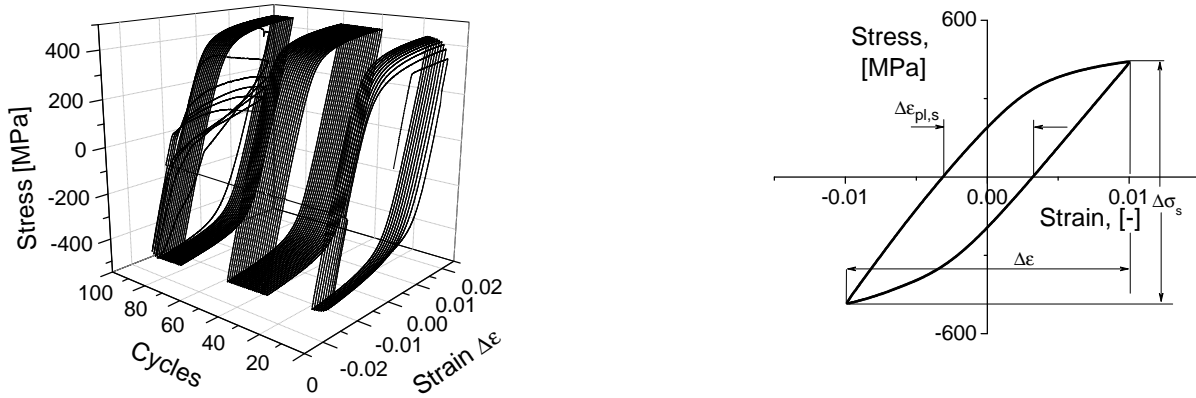
3

Figure 5: a) Cyclic tension-compression response for a specimen subjected to loading with a strain range of 0.035, lasting for 94 cycles (For the sake of clarity, the cycles between 10-30 and 50-75 have been omitted.), b) Stabilized hysteresis for LCF experiments (schematically)

cyclic saturation during which stresses and strains attain steady-state values $\Delta\epsilon_{pl,s}$ and $\Delta\sigma_s$ (Fig. 5(b)). Finally, fatigue damage softening sets in. In this connection, two essential stages can usually be distinguished, mesocrack initiation and crack propagation. The total fatigue life N_R is the sum of the number of cycles necessary to initiate damage N_D and the number of cycles necessary to propagate the crack until final failure N_E (see Fig. 6), i.e.

$$N_R = N_D + N_E . \tag{1}$$

Various semi-empirical models have been proposed for defining a relationship between the lifetime and certain other variables for low cycle fatigue, cf. [18, 19, 20]. The Coffin-Manson plot, see Fig. 7, is the most commonly used approach, which relates the total strain amplitude, $\Delta\epsilon/2$, to the fatigue life N_R and reads

$$\Delta\epsilon/2 = \acute{\epsilon}_f \, (N_R)^c , \tag{2}$$

where $\acute{\epsilon}_f$ and c are the fatigue coefficient and exponent, respectively. The Coffin-Manson parameters, as could be identified as mean values from the respective experiments, are given in Tab. 3 for the L- and the T-direction. Tab. 3 shows the interrela-

Table 3: Coffin-Manson parameters for Al 2024-T351, see Eq. (2)

Orientation	$\acute{\epsilon}_f$ [-]	c [-]	Strain range [%]	Cycles (N_R)
L	0.09838	-0.55	2.5-3.75	48-197
T	0.06421	-0.34127	2.375-4.5	21-145

tionships between the applied strain ranges and the corresponding fatigue lifes. Analogously to the standard Coffin-Manson plot, the moment of damage initiation, measured by the number of cycles N_D, can be plotted in a similar manner. However, as will be explained later, damage initiation is assumed to be

governed by the accumulated plastic strain. Hence, N_D is plotted as a function of $\Delta\epsilon_{pl}$, see Fig. 7(a),(b).

An important observation is that this alloy/structure exhibits a sudden loss of strength. In the monotonic tests upon reaching the ultimate stress (Fig. 6(a)), minute softening is observed before final rupture. Specimens under cyclic loading fail in a similar abrupt manner as well (Fig. 6(b)). Since in ductile materials, the softening phase is longer, the aforementioned observation is an indicator for the brittleness of the material suggesting a rather quasi-brittle material response at the micro-level, see [12].

3. Fractography

After LCF failure of a specimen, the fracture surface morphology was examined with a scanning electron microscope, JEOL JSM-6460LV, operated at an accelerating voltage of 20 kV. The visualizations were made at different magnifications to identify the unique fractographic features, showing the immediate vicinity of the crack initiation site and discriminating the regions of stable and unstable crack extension.

3.1. Uni-axial tension tests

Cracks initiate and propagate in regions where deformation and damage are localized leading eventually either to a flat-faced (fracture surface perpendicular to loading) or slant (shear) fracture, depending on constraints and material. For the considered flat specimens of Al 2024 under monotonic loading, shear rupture occurs. A dominant macrocrack propagates with relatively low necking through the specimen's thickness. The profile of the fracture surface is of so-called slant-shear fracture-type (across the thickness). This kind of failure is typical for thin sheets and small-diameter rods, cf. [25]. The term slant-shear fracture is somewhat misleading, because the angle between the principle axis and the fracture surface was measured on average to be 38°.
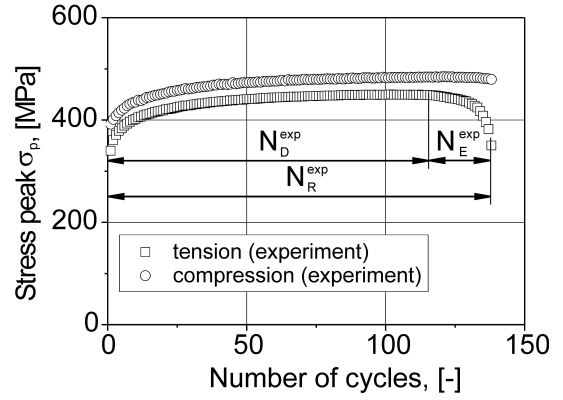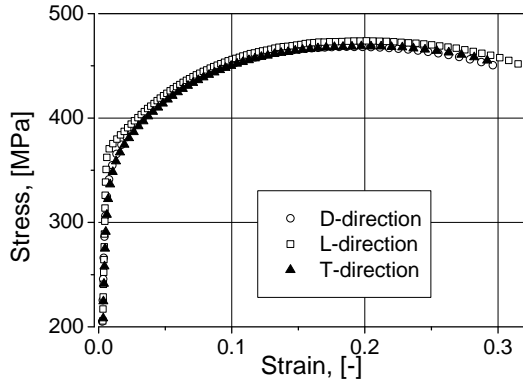
4

Figure 6: a) Stress-strain response for uni-axial monotonic tensile tests; b) peak stresses within the LCF experiments
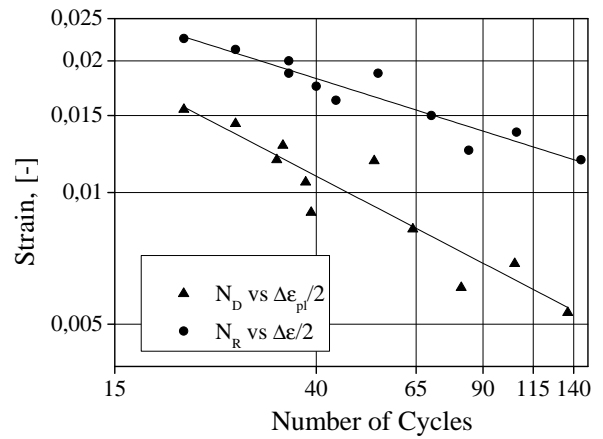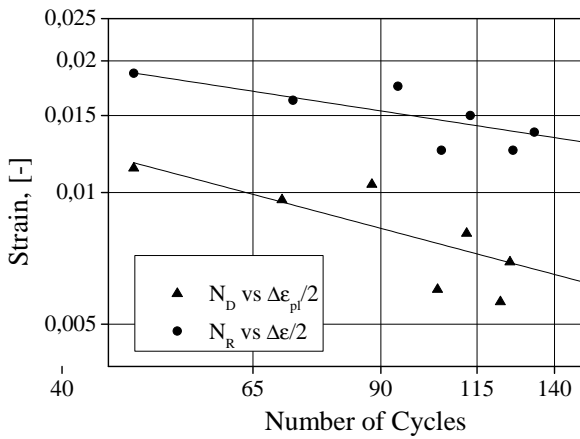

Figure 7: Coffin-Manson diagrams for the specimens according to Fig. 1 tested in: a) L-direction; b) T-direction (model parameters according to Tab. 3)

3.2. Cyclic tests

Typically, fatigue fracture surfaces of aluminum alloy 2024 have a chaotic wavy appearance, cf. [10]. Furthermore, the fracture surface is composed of relatively shiny smooth areas with periodic markings called tire tracks, because they often resemble the tracks left by a tire. For the sake of clarity, the fracture surface is divided into two separate regions: that produced by stable growth and that corresponding to unstable crack growth (Fig. 8). The elliptical front separating such regions
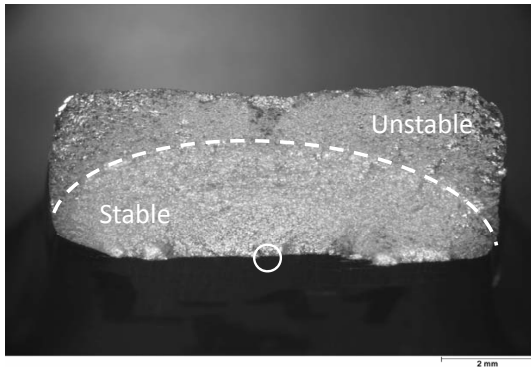

Figure 8: A 60° axial view of the fracture surface; failure after 133 cycles in L-direction, $\Delta\epsilon$=0.0275. The lower small circle indicates the crack initiation site.

grows from the surface across the specimen's thickness. The damage initiation point (discussed in detail in a later section) is close to the center of the ellipse.

A 3D rendering of the images obtained from the SEM shows the initiation point (Fig. 9). The stable crack growth region has
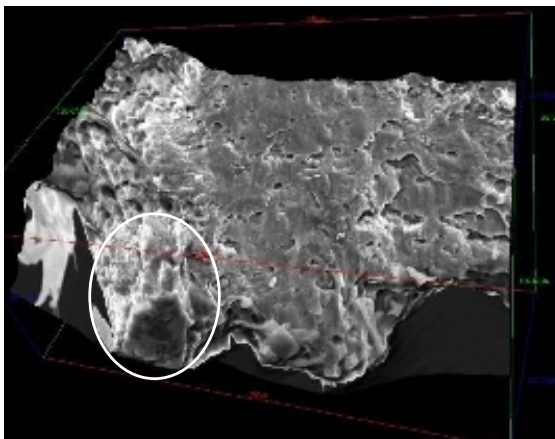

Figure 9: 3D rendered micro-structure of the fracture surface; the left lower circle indicates the crack initiation site; failure after 133 cycles in L-direction, $\Delta\epsilon$=0.0275

a dimple structure with large cavities, characteristic for ductile damage in aluminum alloys. The stable crack grows nearly perpendicular to the loading direction and produces a flat profile. The unstable region has a dimple structure with smaller cavities (Fig. 10a) which are formed during unloading/compression.

Fatigue lines can be observed only in the stable crack growth region (Fig. 10b) with small flat patches, also produced in the compression phase during unloading. The related unstable crack growth region is slanted like that one observed in monotonic loading for the considered flat specimens. The sizes of the unstable and stable crack growth regions vary with loading conditions. For a very high amplitude, restricting the lifetime to a few cycles, the stable crack growth region is smaller as compared to a lower amplitude with a larger number of cycles. There is no observed connection between stable/unstable crack growth regions and trans/intergranular crack propagation. Failure occurs always in a mixed mode without any generalized trend.

3.2.1. Damage Initiation

Material inhomogeneities are common fatigue crack nucleation sites in aluminum alloys, cf. [26, 27]. Inhomogeneities include constituent particles and micropores as intrinsic properties as well as surface features like scratches. In thin sheet aluminum 2024-T351, the rolling of the material has eliminated any microporosity and in the absence of surface scratches, fatigue cracks initiate at constituent particles. Constituent particles generally range in size from 1-40 μm, see [11], and contribute to the strength of the alloy. During high strain processing of thick plates into sheet material, many of these particles break and the larger ones are broken into clusters of smaller particles. If the material is subjected to fatigue loading, cracks emanating from the constituent particles grow into the surrounding aluminum matrix and continue to propagate.

The nucleation of fatigue cracks represents an important stage in the damage evolution process in cyclically loaded materials. In homogeneous materials without appreciable macroscopic defects, the surface of the material plays a prominent role in fatigue crack nucleation. As a matter of fact, the majority of fatigue cracks initiate at the surface, cf. [28]. If macroscopic and microscopic defects (e.g. inclusions, holes and non-coherent precipitates) are present, the interface between the defects and the matrix is a potential site of crack nucleation.

Fig. 11 shows the profile analysis of a fracture surface. Large cavities were found at the surface of the broken specimen and a cavity produced by a particle-up-rooting can be seen close to the initiation site of the fatigue crack. Area analysis (Fig. 11) revealed that the particle sizing is on average 10-20 μm near the surface. As expected, the lifetime is roughly inversely proportional to particle sizing. This implies, the bigger the particle, the sooner damage initiates and the less resistant the material.

4. A ductile-brittle damage model

The experimentally observed quasi-brittle material response of flat sheets of Al 2024 can be naturally captured by a coupled ductile-brittle damage model. Such a material model was recently proposed in [12, 32]. For getting further insight into the mechanical response of Al 2024-T351 accompanying finite element simulations based on this constitutive model are performed. As introduction, the thermodynamically consistent framework proposed in [12, 32] will be briefly described in
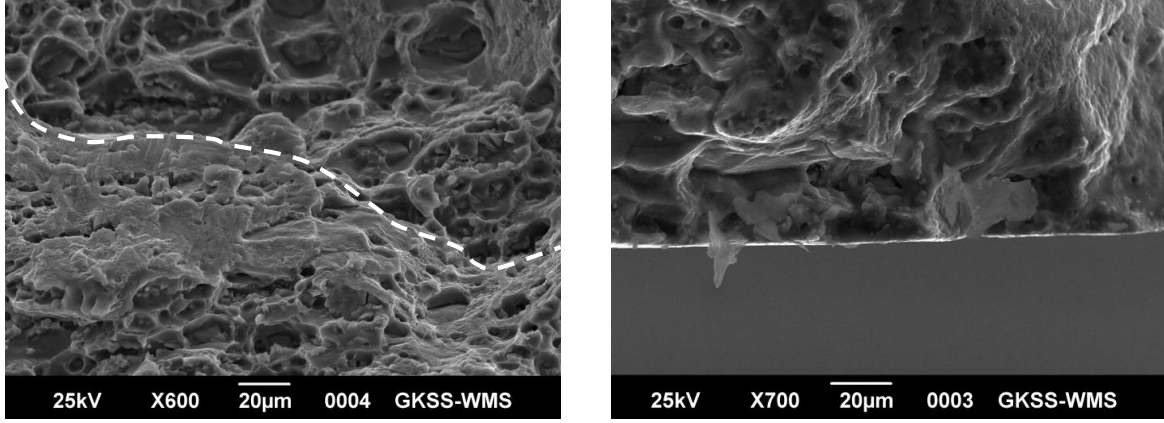
Figure 10: a) Transition path dividing stable (below) and unstable (above) crack growth regions, shown in white; b) Crack initiation site with fatigue lines; failure after 133 cycles in L-direction, $\Delta\epsilon$=0.0275
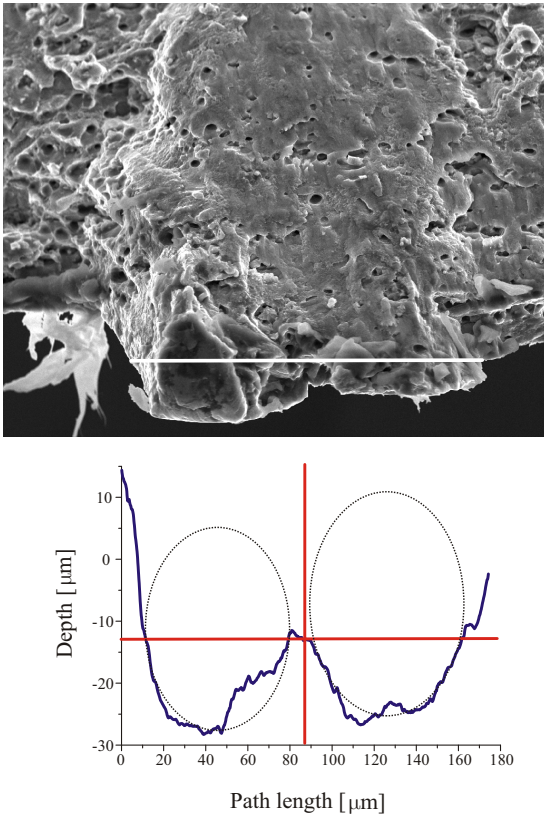

Figure 11: (above) SEM fractograph of the failure surface after 133 cycles in L-direction, $\Delta\epsilon$=0.0275. The line defines the analyzed path; (below) Profile analysis associated with the above path showing two big cavities at the surface

what follows. Throughout this section, a geometrically linear setting is used where the global strains ϵ are decomposed according to $\epsilon = \epsilon^e + \epsilon^p$ with ϵ^e and ϵ^p being its elastic and plastic parts. As far as the notation is concerned, the superscript "p" signals variables associated with plasticity, while the superscript "b" represents variables corresponding to quasi-brittle

damage accumulation.

4.1. Stored energy

The model advocated in [12, 32] is based on a combination of the by now classical approach advocated by Lemaitre & Desmorat [13] and a novel material law for quasi-brittle damage accumulation. Assuming an additive decomposition of the Helmholtz energy Ψ into the different damage modes, Ψ reads

$$\Psi = (1 - D) Y + H_\Gamma \frac{\alpha_\Gamma^2}{2} \tag{3}$$

with

$$Y := \left(\frac{\epsilon^e : \mathbb{C} : \epsilon^e}{2} + H_k \frac{\|\alpha_k\|^2}{2} + H_i \frac{\alpha_i^2}{2} \right). \tag{4}$$

Here, $D \in [0; D_{\mathrm{crit}}]$ is a scalar-valued damage parameter, Y is the Helmholtz energy of the un-damaged solid, $\mathbb{C}$ is the fourth-order elasticity tensor, H_k is the kinematic hardening modulus, H_i is the isotropic hardening modulus, α_k is the strain-like internal variable associated with kinematic hardening, its counterpart for isotropic hardening is denoted as α_i, H_Γ is the hardening modulus corresponding to quasi-brittle damage accumulation and α_Γ is the respective internal variable. Assuming an additive decomposition of the driving force governing damage accumulation is equivalent to the split

$$D = \gamma^p D^p + \gamma^b D^b , \quad \text{with} \quad \gamma^b := 1 - \gamma^p, \tag{5}$$

where γ^p and γ^b are the corresponding composition factors. With assumption (5), the driving force energetically conjugate to D is given by $Y = -\partial_D \Psi = Y^p + Y^b$ with

$$Y^p = -\partial_{D^p} \Psi = \gamma^p Y \quad \text{and} \quad Y^b = -\partial_{D^b} \Psi = \gamma^b Y . \tag{6}$$

4.2. Space of admissible stress states

In line with classical plasticity theory, the space of admissible states is defined by a yield function.

4.2.1. Plastic deformation

Concerning plastic deformation, the von Mises-type yield function

$$\phi^p = \sqrt{\frac{3}{2}\mathrm{dev}(\tilde{\boldsymbol{\sigma}} - \tilde{\boldsymbol{Q}}_k) : \mathrm{dev}(\tilde{\boldsymbol{\sigma}} - \tilde{\boldsymbol{Q}}_k)} - (\tilde{Q}_i + Q_0^{eq}) \leq 0 \tag{7}$$

is adopted where Q_0^{eq} is the initial yield limit. This yield function is formulated in terms of effective stress-like variables indicated by the tilde sign. Introducing the stresses $\boldsymbol{\sigma}$ and the stress-like internal variables conjugate to $\boldsymbol{\epsilon}^p$, $\boldsymbol{\alpha}_k$, α_i in standard manner as

$$\boldsymbol{\sigma} = \partial_\epsilon \Psi = -\partial_{\epsilon^p}\psi, \quad \boldsymbol{Q}_k = -\partial_{\alpha_k}\Psi, \quad Q_i = -\partial_{\alpha_i}\Psi, \tag{8}$$

their respective effective counterparts are given by

$$\tilde{\boldsymbol{\sigma}} = \frac{\boldsymbol{\sigma}}{(1-D)}, \;\; \tilde{\boldsymbol{Q}}_k = \frac{\boldsymbol{Q}_k}{(1-D)}, \;\; \tilde{Q}_i = \frac{Q_i}{(1-D)} \;. \tag{9}$$

It bears emphasis that within the original model by Lemaitre & Desmorat [13] only the stresses are used as effective quantities.

4.2.2. Quasi-brittle damage accumulation

Analogously to the plastic deformation, quasi-brittle damage accumulation is also governed by a yield-type function. In line with Eq. (7), this function is assumed as

$$\phi^b = \frac{|(Y^b)^N - \Gamma|}{S_2} - Q_{b0} \leq 0 \;. \tag{10}$$

According to Eq. (10) this function is formulated in terms of energy-like variables such as the energy release rate Y^b. Γ is a so-called shift tensor, which defines an alternate threshold, while Q_{bo} represents a constant threshold, both defining damage activation. N and S_2 are material parameters.

4.3. Evolution equations

In case of fully elastic states, the stresses can be directly computed by using Eq. (8)$_1$. Otherwise, the updated plastic deformation and the updated damage accumulation have to be determined first. They are based on the evolution equations discussed next.

4.3.1. Plastic deformation

If plastic loading is signaled by $\phi^p = 0$ and $\dot{\phi}^p = 0$, where the superposed dot denotes the material time derivative, the evolution equations of the internal variables associated with ductile deformation are derived from the convex plastic potential

$$\bar{\phi}^p = \phi^p + \frac{B_k}{H_k}\frac{\tilde{\boldsymbol{Q}}_k : \tilde{\boldsymbol{Q}}_k}{2} + \frac{B_i}{H_i}\frac{\tilde{Q}_i^2}{2} + \frac{(Y^p)^M}{MS_1(1-D)} \;. \tag{11}$$

The additional quadratic terms, depending on the stress-like internal variables $\tilde{\boldsymbol{Q}}_k$ and $\tilde{Q}_i$, are associated with nonlinear kinematic and isotropic hardening of Armstrong-Frederick-type, while the last term corresponds to the evolution law of the damage-related variable D^p. In Eq. (11), B_k, B_i, M and S_1 are material

parameters. With Eq. (11) and following the framework of generalized standard materials (see [23]), the evolution equations are postulated to be

$$\dot{\boldsymbol{\epsilon}}^p = \lambda^p\,\partial_{\boldsymbol{\sigma}}\bar{\phi}^p, \quad \dot{\boldsymbol{\alpha}}_k = \lambda^p\,\partial_{\boldsymbol{Q}_k}\bar{\phi}^p, \quad \dot{\alpha}_i = \lambda^p\,\partial_{Q_i}\bar{\phi}^p \tag{12}$$

and

$$\dot{D}^p = \lambda^p\,\partial_{Y^p}\bar{\phi}^p \;. \tag{13}$$

Here, $\lambda^p \geq 0$ is the plastic multiplier. As shown in [12, 32], convexity of the plastic potential $\bar{\phi}^p$ guarantees a positive dissipation in case of plastic loading. Thus, the second law of thermodynamics is automatically fulfilled. The crack closure effect is accounted for in case of compression by reducing the damage evolution (13) by a factor of 0.2, cf. [23].

4.3.2. Quasi-brittle damage accumulation

Considering again the framework of generalized standard materials, cf. [23], the evolution equations are derived from the convex damage potential

$$\bar{\phi}^b := \phi^b + \frac{B_\Gamma}{H_\Gamma}\frac{\Gamma^2}{2} \tag{14}$$

where B_Γ is an additional material parameter. Using Eq. (14), the evolution of the quasi-brittle damage related internal variables are assumed to be of the type

$$\dot{D}^b = \lambda^b\frac{\partial\bar{\phi}^b}{\partial Y^b} = \lambda^b\frac{\mathrm{sign}((Y^b)^N - \Gamma)}{S_2}N\,(Y^b)^{N-1}\,, \dot{\alpha}_\Gamma = \lambda^b\frac{\partial\bar{\phi}^b}{\partial\Gamma} \tag{15}$$

if loading is signaled by $\phi^b = 0$ and $\dot{\phi}^b = 0$. In Eq. (15), λ^b is the damage multiplier. For guaranteeing a positive damage evolution, damage growth is considered for a half-cycle only, i.e., in case of a positive sign of $(Y^b)^N - \Gamma$.

4.4. Damage initiation and the formation of a mesocrack

While plastic deformation occur, whenever the loading conditions $\phi^p = 0$ and $\dot{\phi}^p = 0$ are fulfilled, damage initiation is governed by an additional criterion. Following [13], damage is assumed to initiate when the energy associated with cold plastic work w_s reaches the threshold w_D, cf. [13, 35]. This assumption complies well with the empirical Coffin-Manson rule in which the fatigue lifetime depends on the amplitude of the (plastic) strains. The modified energy related to cold plastic work w_s proposed in [13, 35] reads

$$w_s = \int_0^{t_{n+1}} \left(R_\infty(1 - e^{-br})\frac{A}{m}r^{\frac{1-m}{m}}\dot{r} \right) \mathrm{d}t + \frac{H_k}{2}(\boldsymbol{\alpha}_k : \boldsymbol{\alpha}_k) \tag{16}$$

where A and m are material parameters, r is the accumulated plastic strain and R_∞ and b are related to isotropic hardening, cf. [12]. Based on the driving force w_s (strictly speaking, a driving energy), damage initiates, if

$$w_s > w_D. \tag{17}$$

8

The threshold w_D is a material parameter.

Once criterion (17) is met, damage evolution is governed by the yield functions (7) and (10) as well as by the evolution equations (13) and (15)$_1$. Physically speaking, damage initiation corresponds to the formation of microcracks. These microcracks propagate and coalesce leading eventually to a mesocrack. Analogously to [13], it is assumed that such a mesocrack forms, if the damage variable D reaches the threshold D_{crit}. Within the numerical simulations, D_{crit} has been set to $D_{crit} = 0.23$.

4.5. A variationally consistent reformulation

Since the evolution equations of the constitutive model described in the present section fall into the framework of generalized standard materials (see [23]), the resulting overall model is thermodynamically consistent and fulfills the second law of thermodynamics. Although the underlying evolution equations are non-associative ($\bar{\phi}^p \neq \phi^p$, $\bar{\phi}^b \neq \phi^b$) it was recently shown in [32] that the model possesses even a variational structure. Without going too much into detail, this structure allows to compute all state variables jointly and conveniently from minimizing an incrementally defined energy $\mathcal{E}$ which turns out to be the stress power, i.e.

$$\dot{X} = \arg\inf_{\dot{X}} \mathcal{E}, \qquad \text{with} \qquad X = \{\boldsymbol{\epsilon}^p, \boldsymbol{\alpha}_k, \alpha_i, \alpha_\Gamma, D\} \tag{18}$$

and

$$\boldsymbol{\sigma} = \partial_{\boldsymbol{\epsilon}} \inf_{\dot{X}} \mathcal{E}. \tag{19}$$

Based on this variational structure, efficient finite element implementations can be derived, cf. [32]. Such an implementation has also been employed for the numerical analyses presented in the following sections.

5. Material parameter identification strategy

The identification of the model parameters is accomplished in five tasks, following a step-by-step procedure. This method is used for the T- as well as for the L-direction. In the following, the steps defining the identification strategy are briefly described.

1. The elastic material parameters and the yield limit (E,ν,σ_y) are inferred from the monotonic tensile curves. Concerning the evolution of quasi-brittle damage, the admissible assumptions $N = 1.25$ and $S_2 = N$ are made, cf. [12]. Further following [12], Q_{b0} can be computed from $Q_{b0} = [\gamma^b (\sigma^f)^2/2E]^N/N$. Taking an average value of σ^f=62.5 MPa, Q_{b0} is computed as $0.0009122838\ (\text{MJ/m}^3)^N$ ($\gamma^b = 1$, $E = 70000$ MPa as average value was taken for both T- and L-directions, N=1.25). Further details are omitted here. They can be found in [12].

2. The isotropic hardening (H_i, B_i) and nonlinear kinematic hardening parameters (H_k, B_k) are calibrated considering the experimental data for a strain amplitude of $\Delta\epsilon = 0.0375$ (before damage initiation). For that purpose, the respective least squares problem is solved.

3. For determining the set of parameters A, m and w_D defining the plastic stored energy (16) driving damage initiation, the objective function

$$\{A, m, w_D\} = \arg\min_{\{A,m,w_D\}} \left(\sum_{i=1}^{n} \text{abs}(\log N_{D,i}^{exp} - \log N_{D,i}^{sim}) \right) \tag{20}$$

is minimized, where $N_{D,i}^{exp}$ are the experimentally observed cycles and $N_{D,i}^{sim}$ are the numerically simulated counterparts at the onset of damage initiation, respectively. n is the number of experiments with different strain amplitudes.

4. The material parameters governing ductile damage (M and S_1) are found by comparing the numerically predicted lifetimes to their experimentally observed counterparts. Within the respective optimization problem

$$\{M, S_1\} = \arg\min_{\{M,S_1\}} \left(\sum_{i=1}^{n} \text{abs}(\log N_{R,i}^{sim} - \log N_{R,i}^{exp}) \right), \tag{21}$$

quasi-brittle material degradation is ignored ($\gamma^b = 0$). As a consequence, step 1 up to step 4 can also be used for calibrating the by now classical model by Lemaitre & Desmorat [13].

5. Finally, the composition factor γ^b as well as the parameters B_Γ and H_Γ defining the quasi-brittle damage model are computed from the optimization problem

$$\{B_\Gamma, H_\Gamma, \gamma^b\} = \arg\min_{\{B_\Gamma,H_\Gamma,\gamma^b\}} \left(\sum_{i=1}^{n} \text{abs}(\log N_{R,i}^{sim} - \log N_{R,i}^{exp}) \right). \tag{22}$$

The material parameters obtained from the described material parameter identification strategy are summarized in Tab. 4.

Table 4: Calibrated material parameters for Al 2024-T351 sheets, 4 mm thickness

Elasticity		
Orient.	E [MPa]	ν [-]
L	71000	0.3
T	70000	0.3

Plasticity				
Orient.	Q_0^{eq} [MPa]	H_i[MPa]	B_i [-]	H_k [MPa]	B_k [-]
L	345	501.252	5.01252	3333.33	90.0
T	280	1050.766	11.0606	16666.66	265.0

Stored plastic energy		
Orient.	m [-]	A [-]	w_D [MJ/m³]
L	4.964	9.7e-03	0.7247
T	2.479	10.6e-03	1.41

Damage evolution					
M [-]	S_1 [-]	H_Γ [-]	B_Γ [MPa]	γ^b [-]	D_{crit} [-]
1.0511	2.12	0.0515	200.5	0.45	0.23
0.9475	2.07	0.115	43.39	0.45	0.23
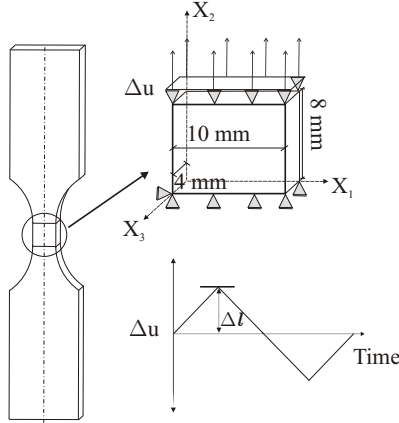
Figure 12: Sketch of the specimen and the loading conditions used in the finite element simulations

Orientation	$\Delta\varepsilon$ [%]	Number of cycles		
		Experiment	Simulation - N_E^{sim}	
		N_E^{exp}	ductile	coupled
L	3.75	4	12.0	10.0
	3.5	8	11.26	9.62
	3.0	8	13.59	10.5
	2.75	10	17.755	11.0
T	3.25	5	7.0	6.0
	3.0	6	17.22	16.0
	2.5	7	23.405	20.45
	2.375	9	25.82	21.4875

6. Numerical analysis of LCF in Al 2024-T351

Based on the calibration of the material parameters, the predictive capabilities of the constitutive model suitable for the analysis of sheets of high-strength aluminum alloys are demonstrated in the present section. While Subsection 6.1 is associated with the flat specimens experimentally analyzed in Section 2, a more complex engineering structure is considered in Subsection 6.2. As a prototype of such a structure, a stringer-skin connection of a fuselage is chosen.

6.1. Flat specimens

The lifetimes of the flat specimens experimentally analyzed in Section 2 are computed here by using the ductile-brittle damage model discussed in the previous section. For the respective finite element simulations, a three-dimensional model representing a quarter of the specimen's gauge section is considered imposing a two-fold symmetry condition (X_1 and X_2). Despite the fact that the specimen's thickness is comparably small, the simulations are done using a three-dimensional discretization. A coarse mesh is used with mesh refinement at the expected regions of stress concentration which allows a good simulation of necking and constraints caused by damage localization. Tri-linear finite elements (3D bricks with 8 nodes) are used in the discretization. The triangulation consists of eight elements across the thickness. A typical dimension of a finite element is 0.2 mm in longitudinal and transversal and 0.5 mm in thickness-direction. The specimens are loaded under displacement control with a prescribed linear amplitude function for cyclic loading (Fig. 12).

The 3D specimens are meshed with a geometrical imperfection. A slight hourglass shape is used for localizing damage at the middle-plane. Clearly, mesh size and design are critical for damage calculations with softening, cf. [6, 29, 30]. As mesh-defining quantity, the total fracture energy is related to the damage process in the respective zone, cf. [29, 31]. Hence, the mesh size can be interpreted as some micro-structural characteristic length scale (e.g. inter-particle spacing or grain size).

Within the computations, the calibrated material parameters summarized in Tab. 4 are used. The numerically predicted lifetimes are given in Tab. 5. For the sake of comparison, a purely ductile damage model in the spirit of [13] is also considered. Since both models are equivalent before damage accumulation, only the numbers of cycles within the softening regime (N_E^{sim}) are given. According to Tab. 5, a purely ductile damage model leads to a significant overestimation of the lifetime. By way of contrast, the fully coupled ductile-brittle approach captures the underlying physical processes in a more realistic manner and thus, leads to better agreements with the experiments. A graphical illustration of the numerical results for the L-direction, together with the experimentally observed counterparts, is shown in Fig. 13. As evident, the coupled model yields more realistic
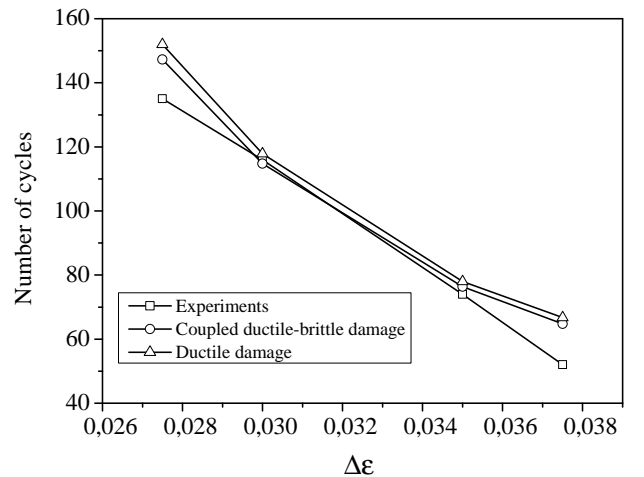

Figure 13: Lifetime prediction for the flat specimen (L-direction), see Fig. 12

lifetimes.

6.2. Stringer-skin connection of a fuselage

The whole visible part of an airplane is constituted of stiffening panels, i.e. an outer thin sheet (skin) with generally orthogonally arranged integral or fastened stiffeners. The stringers and frames in a fuselage shell are sketched in Fig. 14. The fas-
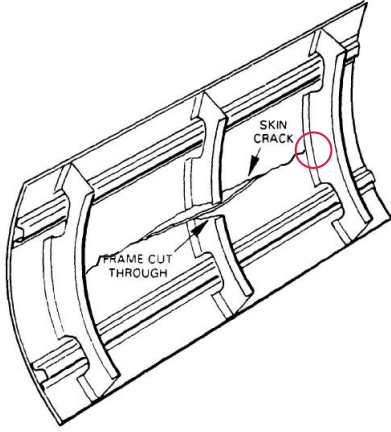

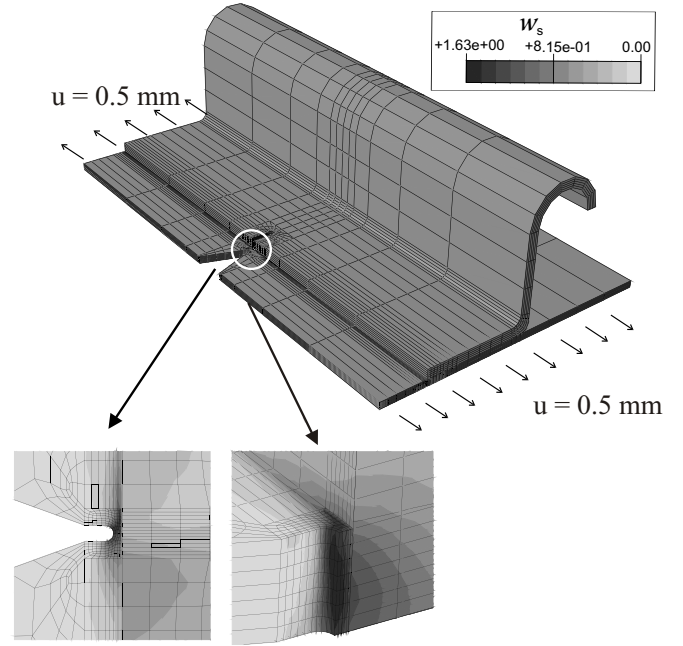Figure 14: Fuselage stiffened panel with a longitudinal skin crack over a broken frame [41]

Figure 15: Distribution of the stored plastic energy w_s driving damage initiation. Lower left hand side: crack front at the elliptical notch (top view); lower right hand side: profile of plastic stored energy (side view). The relative position of the analyzed stringer-skin connection within the fuselage section is marked by the circle in Fig. 14

tened stiffeners can be riveted, adhesive bonded or welded to the skin [40]. Clearly, the design of such structural components requires the estimation of their lifetimes. In the past, different, mostly ad-hoc, concepts have been considered for that purpose. Since it was experimentally observed that the stringer failure is driven by a low-cycle fatigue mechanism [42], the lifetime can be naturally estimated by using the constitutive model described in the previous sections.

Although the stringer is bonded to the skin, the whole assembly is considered as homogeneous and no special contact conditions have been defined within the respective finite element simulations. Despite the fact that a bonded stringer-skin assembly performs better with regard to damage tolerance, the purpose of this simulation was not to evaluate/judge the bonding strength. In industrial practice and at the laboratory testing stage only through-the-thickness cracks are used, i.e., the crack front is always considered straight. To model such a situation, an elliptical through-thickness notch is taken here as precrack ahead of the stringer, see Fig. 15. The assumption of such a blunt notch reducing stress singularities is very practical from a modeling point of view. Otherwise damage would already evolve from the beginning. Furthermore, it is important to note that the numerical analyses were not intended to obtain the crack propagation profile. More explicitly, focus was on damage initiation (propagation of micro-cracks).

The structure shown in Fig. 15 has been cyclically loaded displacement controlled under symmetric load condition ($R = -1$). A very fine mesh especially around the elliptical notch has been generated. With one exception, the material parameters given in Tab. 4 have been used for the numerical analysis. This exception is the plastic energy threshold (w_D) which has been altered to a value of 1.62. This value has been taken from the

uni-axial simulations (L-direction).

The results of the finite element simulation are shown in Fig. 15. The coupled damage model predicts microcrack initiation in the assembly after 60 load cycles. Subsequently, damage evolves fast to the critical value.

Without doubt, crack propagation is also important for estimating the lifetime of structural components. For that purpose, however, the constitutive model has to be modified. Such an extension is beyond the scope of the present paper.

7. Conclusions

In the present paper, the low-cycle fatigue behavior of flat sheets of aluminum Al 2024-T351 was carefully analyzed. For that purpose, material characterization was combined with material modeling. For allowing symmetric strain amplitudes (R=-1) within the cyclic loading experiments, a floating anti-buckling guide has been proposed which successfully prevents buckling at high compressive loading without affecting adversely the mechanical behavior of the specimen. Based on the subsequent fractography it was shown that Al 2024 as a sheet exhibits a mixed-mode fracture behavior ranging between brittle and ductile. Furthermore, damage initiates at bigger particles/inclusions at the surface of the specimen and propagates with a spherical crack front. A transition zone between the fracture mechanism was also observed (stable/unstable crack growth regions). Additionally, experimental macroscopic results confirmed a rapid damage evolution up to failure. All these observations suggested that a ductile damage model alone is not sufficient for

predicting the lifetime of this alloy accurately enough.

For capturing the complex ductile-brittle damage accumulation of aluminum Al 2024-T351 sheets, a recently published coupled approach was considered. Within this approach, a modified model originally advocated by Lemaitre [13] suitable for the analysis of ductile damage was combined with a model for quasi-brittle damage evolution. The parameters of that model were optimized by means of a staggered identification strategy. Comparisons between the predictions computed by the final model and experiments for flat specimens showed a very good agreement. In particular, the estimated lifetimes are more realistic than those based on a purely ductile damage model. That confirmed the quasi-brittle nature of damage accumulation in flat sheets of Al 2024-T351.

As an outlook and for demonstrating the robustness and efficiency of the finite element model, a complex engineering problem was also analyzed. More precisely, damage initiation in a stringer-skin connection of a fuselage was considered. While in the past, different, mostly ad-hoc, concepts have been considered for designing such structures to reach a desired lifetime, the combination of careful material characterization and physically sound modeling as discussed in the present paper allows to put this design process on more solid grounds.

References

[1] F. McClintock, A criterion for ductile fracture by the growth of holes, J. Appl. Mech. 35 (1968) 363–371.

[2] J. Rice, D. Tracey, On ductile enlargement of voids in triaxial stress fields, J. Mech. Phys. Solids 17 (1969) 210–217.

[3] J. Rice, D. Tracey, On the Ductile Enlargement of Voids in Triaxial Stress Fields, J Mech Phys Solid 17 (1969) 201–217.

[4] A. Gurson, Continuum theory of ductile rupture by void nucleation and growth: part I—yield criteria and flow rules for porous ductile media, J. Mech. Mater. Technol. 99 (1977) 2–15.

[5] A. Needleman, J. Rice, Limits to ductility by plastic flow localization, Plenum, New York, 1978, Ch. Mechanics of Sheet Metal Forming, pp. 237–265.

[6] V. Tvergaard, A. Needleman, Analysis of the cup-cone fracture in a round tensile bar, Acta Metall. 32 (1984) 157–169.

[7] L. Kachanov, Time of the Rupture Process under Creep Conditions, Isv. Akad. Nauk. SSR. Otd Tekh. Nauk. 8 (1958) 26–31.

[8] D. Steglich, W. Brocks, J. Heerens, T. Pardoen, Anisotropic ductile fracture of Al alloys, Eng Fract Mech 75 (2008) 3692–3706.

[9] N. Bonora, D. Gentile, A. Pirondi, G. Newaz, Ductile damage evolution under triaxial state of stress, theory and experiments, International Journal of Plasticity 21 (2005) 981–1007.

[10] S. Khan, A. Vyshnevskyy, J. Mosler, Low cycle lifetime assessment of Al2024 alloy, Int J Fatigue 32, Issue 8 (2010) –.

[11] A. Vyshnevskyy, S. Khan, J. Mosler, An investigation on low cycle lifetime of Al2024 alloys, J Key Engng Mater 417-418 (2009) 289–292.

[12] O. Kintzel, S. Khan, J. Mosler, A novel isotropic quasi-brittle damage model applied to LCF analyses of Al2024, International Journal of Fatigue 32 (2010) 1948–1959.

[13] J. Lemaitre, R. Desmorat, Engineering damage mechanics, Springer, Berlin, 2005.

[14] Harris, Structural integrity of aging airplanes, in: International Symposium on Structural Integrity of Aging Aeroplanes, pp. 141-152, Springer, Atlanta, 1990.

[15] M. Milan, D. Spinelli, W. Bose, Fatigue and monotonic properties of an interstitial free steel sheet (fmpif), International Jounal of Fatigue 23(2) (2001) 129–133.

[16] K. Fredriksson, A. Melander, M. Hedman, Influence of prestraining and aging on fatigue properties of high-strength sheet steels., International Jounal of Fatigue 10(3) (1988) 139–151.

[17] K. Biswas, Problems and feasibilities of testing the cyclic behaviour of thin sheet steels, Steel Research 64(8-9) (1993) 407–413.

[18] J. Morrow, T. Johnson, Correlation between cyclic strain range and low-cycle fatigue life of metals, Materials Research and Standards 5(1) (1965) 30–37.

[19] B. Tomkins, Fatigue crack propagation - an analysis, Philosophical Magazine 18(155) (1968) 1041–60.

[20] A. Saxena, S. Antolovich, Fatigue crack-propagation and substructures in a series of polycrystalline cu-al alloys, Metallurgical Transactions a-Physical Metallurgy and Materials Science 6(9) (1975) 1809–28.

[21] S. Horibe, C. Laird, Orientation and history dependence of cyclic deformation in al-cu single-crystals containing theta' precipitates, Acta Metallurgica 31(10) (1983) 1567–79.

[22] H. Biermann, B. vonGrossman, T. Schneider, S. Mechsner, H. Feng, H. Mughrabi, Microstructural analysis of an industrial single-crystal aeronautic turbine blade - evaluation of local stress, Zeitschrift Fur Metalkunde 88(8) (1997) 666–675.

[23] J. Lemaitre, A course on damage mechanics, Springer, Berlin, 1992.

[24] Z. Li, Y. Zhao, S. Schmauder, M.Dong, Quantitative characterization of microcracking in brittle materials by finite element modeling, Eng. Fract. Mech. 51(3) (1995) 497–504.

[25] J. Besson, D. Steglich, W. Brocks, Modeling of plane strain ductile rupture, Int. J. Plast. 19 (2003) 1517–1541.

[26] K. Tanaka, A theory of fatigue crack initiation at inclusions, Metallurgical Transactions A-Physical Metallurgy and Materials Science 13(1) (1982) 117–123.

[27] C. Bowles, J. Schijve, Role of inclusions in fatigue crack initiation in an aluminum alloy, International Jounal of Fracture 9(2) (1973) 171–79.

[28] J. Man, K. Obrtilk, J. Polak, Study of surface relief evolution in fatigued 316l austenitic stainless steel by AFM, Materials Science and Engineering a-Structural Materials Properties Microstructure and Processing 351(1-2) (2003) 123–132.

[29] G. Rousselier, Ductile fracture models and their potential in local approach of fracture, Nucl. Eng. Des. 105 (1987) 97–111.

[30] L. Xia, C. Shih, J. Hutchinson, A computational approach to ductile crack growth under large scale yielding conditions, J. Mech. Phys. Solids 43(3) (1995) 389–413.

[31] A. Gullerud, X. Gao, R. D. J. R. Haj-Ali, Simulation of ductile crack growth using computational cells: numerical aspects, Eng. Fract. Mech. 66 (2000) 65–92.

[32] O. Kintzel, J. Mosler, A small-strain, isotropic coupled ductile-brittle damage model solved by energy minimization for dissipative solids, International Jounal for Numerical Methods In Engineering In press.

[33] V. Radhakri, An analysis of low cycle fatigue based on hysteresis energy, fatigue & Fracture of Engineering Materials & Structures 3(1) (1980) 75–84.

[34] V. Kliman, M. Bily, Hysteresis energy of cyclic loading, Materials Science and Engineering 68(1) (1984) 11–18.

[35] J. Lemaitre, R. Desmorat, M. Sauzay, Anisotropic damage law of evolution, European Journal of Mechanics a-Solids 19(2) (2000) 187–208.

[36] P. Paris, M. Gomez, W. Anderson, A Rational Analytic Theory of Fatigue, The Trend in Engineering 13 (1961) 9–14.

[37] ASM-Handbook, Fatigue and Fracture, Volume 19, ASM, Materials Park, 1996.

[38] J. Neadler, R. Mead, A simplex method for function minimization, Computer J. 7 (1965) 308–313.

[39] T. Morgeneyer, M. Starink, I. Sinclair, Evolution of voids during ductile crack propagation in an aluminium alloy sheet toughness test studied by synchrotron radiation computed tomography, Acta Materialia 56(8) (2008) 1671–79.

[40] M. Niu, Airframe structural design, Hong Kong Conmilit Press Ltd., Hong Kong, 1999.

[41] T. C. FAA, Damage tolerance assessment handbook volume i: Introduction fracture mechanics fatigue crack propagation, Tech. rep., U.S. Department of Transportation - Federal Aviation Administration (1993).

[42] I. Meneghin, Damage tolerance assessment of stiffened panels:, Tech. rep., University of Bologna (2010).